Nano Research

Open Access

Research Article

Self-supported nano-Ru anchored copper-cobalt oxide nanoplates for efficient electrocatalytic removal of low concentration nitrate

Jiao Hu[1,5], Jun Zhou[1,2], Menglin Zhou[1], Yao Huang[2] ✉, Xuguang An[3], Dong Fang[4] ✉, and Guangzhi Hu[1,5] ✉

[1] *Institute of International Rivers and Eco-Security, Yunnan Key Laboratory of Ecological Protection and Resource Utilization of River-Lake Networks, School of Ecology and Environmental Science, Yunnan University, Kunming 650504, China*
[2] *School of Chemical Engineering, Yunnan Open University, Kunming 650223, China*
[3] *School of Mechanical Engineering, Chengdu University, Chengdu 610106, China*
[4] *Faculty of Materials Science and Engineering, Kunming University of Science and Technology, Kunming 650093, China*
[5] *Southwest United Graduate School, Kunming 650092, China*

Cite this article: *Nano Research*, **2026**, *19*, 94908836. https://doi.org/10.26599/NR.2026.94908836

ABSTRACT: Nitrate (NO_3^-) contamination in water adversely affects human health and the ecosystem. Electrochemical methods can remediate environmental NO_3^- pollution. This study developed Ru-Cu_2O/Co_3O_4@copper foam (CF), a hierarchical catalyst comprising a CF substrate, Cu-Co layered double hydroxide (LDH) nanosheets, and ultrasmall Ru nanoparticles. Traditional characterization confirmed its active component composition and chemical oxidation states. Studies on electrochemical NO_3^- reduction have evaluated catalytic efficacy under various conditions. This catalyst exhibits exceptional efficacy in NO_3^- catalysis. At −1.61 V vs. Ag/AgCl, it converts 50 mg/L NO_3^-–N into pure, environmentally friendly N_2 after 4 h, achieving a 98.44% removal efficiency and approximately 100% selectivity, enabling efficient NO_3^- elimination and green N conversion. Throughout 20 cycles, the removal rate of NO_3^-–N remained consistently high (94.19%–99.53%), whereas N_2 selectivity exhibited excellent stability (93.62%–100%).

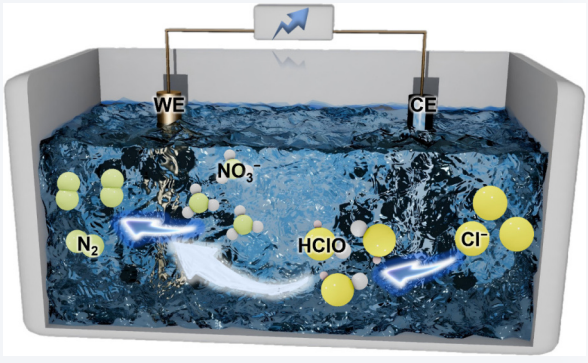

KEYWORDS: nitrate pollution, electrocatalysis, denitrification, N_2 selectivity

1 Introduction

Currently, nitrate (NO_3^-) concentrations in groundwater have exceeded the statutory limits [1–3]. Many rivers and lakes near cities have higher NO_3^- concentrations due to human activity [4, 5]; in rural areas with well-developed agriculture, NO_3^- concentrations in groundwater have reached or exceeded drinking water standards [6–8]; and in areas with severe industrial pollution, NO_3^- concentrations in groundwater are considerably elevated [9]. The rapid accumulation of NO_3^- poses considerable hazards to the environment and human health. In aquatic ecosystems, this accumulation predominantly occurs as eutrophication, leading to excessive algal blooms, water bloom outbreaks, diminished dissolved oxygen levels, and mortality of aquatic organisms [10]. NO_3^- ingested in the food chain can be converted into nitrites (NO_2^-) in the human body, potentially leading to methemoglobinemia and "blue baby syndrome" in infants. Long-term excessive NO_3^- and NO_2^- intake can increase the risk of gastrointestinal cancer in adults [11, 12].

Technologies for the removal of NO_3^- include ion exchange, reverse osmosis, electrodialysis, biological denitrification, chemical reduction, and electrochemical reduction [13–15]. Each strategy has constraints. Physical methods can isolate and concentrate NO_3^- rather than transform it, thereby leading to additional pollution and costly post-treatment processes [16]. Biological methods are ineffective for industrial wastewater and groundwater with minimal biodegradable organic matter, and they require labor-intensive continuous monitoring and operation, limiting their use [17]. Chemical methods require substantial quantities of metal as reducing agents and the incorporation of lime-softened water, which leads to secondary pollution, high costs, and environmental damage, making them inappropriate for large-scale

Received: April 2, 2026; **Revised:** April 29, 2026
Accepted: May 11, 2026

✉Address correspondence to Yao Huang, ynou_hy@163.com; Dong Fang, fangdong@kmust.edu.cn; Guangzhi Hu, guangzhihu@ynu.edu.cn

implementation [18]. Electrochemical reduction of NO_3^- does not require considerable amounts of reducing agents or carbon sources, nor does it generate secondary pollutants [19–21]. This approach employs electrical energy as the main driving factor, enabling efficient and precise conversion of NO_3^- by regulating the active sites of the catalyst. NO_3^- can be converted into N gas (N_2) or beneficial ammonia (NH_3) via multi-electron reduction, thereby mitigating water eutrophication and enhancing N resource recycling. This approach has multiple advantages, such as enhanced denitrification efficiency, ease of use, environmental sustainability, and minimal capital investment [21, 22].

Electrocatalysts are the primary factor affecting reduction efficiency and product selectivity. Contemporary research has predominantly focused on two categories of materials: noble metal catalysts and non-noble metal catalysts. Noble metals, such as Rh, Ru, Pd, and Au, are effective catalysts [23–25]; however, their high cost poses challenges for large-scale industrial use. Under acidic conditions, Pt and Pd produce more adsorbed hydrogen, obstructing the active sites and impeding the reduction process. Noble metal catalysts typically produce NH_3 as a by-product of reduction instead of N_2. Nonprecious metal-based catalysts, such as Cu, Fe, Co, Ni, and Ti, have been intensively studied because of their cost-effectiveness and enhanced electrochemical performance [15, 26, 27]. Nonetheless, individual metal catalysts experience issues, such as metal particle leaching, oxidation, aggregation, and reduced longevity [28]. Conversely, metal oxides and multi-metal systems have superior electrocatalytic performance. Transition metal oxides (including Co-, Cu-, Fe-, Ni-, and Ti-based oxides) have garnered significant interest due to their tunable electronic structures, abundant oxygen vacancies, bimetallic synergistic effects, and high chemical stability, which can effectively address the challenges of sluggish kinetics in multi-step proton-coupled electron transfer and low competitive selectivity in hydrogen evolution reaction (HER). Among single-component oxides, CuO typically converts NO_3^- into nitrites (NO_2^-), whereas Co_3O_4 shows excellent NH_3 synthesis ability. The efficacy of bimetallic oxides (e.g., $CuCoO_x$ and $NiCo_2O_4$) can be augmented through Cu-Co and Ni-Co dual-site synergistic catalysis, heterojunction interface charge transfer, enhanced hydrogen production, and expedited hydrogenation of intermediates [29]. Consequently, through defect engineering, heterostructure fabrication, and heteroatom doping, transition metal oxides can achieve elevated catalytic activity and selectivity, offering an effective and economical solution for wastewater denitrification. Moreover, despite NH_3 being a high-value chemical product, its separation from the solution remains challenging. Consequently, the breakpoint chlorination approach can be employed to transform ammonium ion (NH_4^+) generated during the reaction phase into non-toxic N_2, achieving complete denitrification [30, 31].

In this study, copper foam (CF) self-supporting Ru-Cu_2O/Co_3O_4 catalysts were prepared by hydrothermal synthesis, impregnation, and tube furnace annealing. Ru-Cu_2O/Co_3O_4 @CF showed excellent electrocatalytic NO_3^- reduction performance. The effects of different factors (potential, pH, catalyst, initial concentration of NO_3^-, etc.) on the catalytic performance were systematically studied. NH_3 is a thermodynamically more favorable product of nitrate reduction, but it is very soluble in water and difficult to separate from it, which brings difficulties to the subsequent treatment of water. Therefore, with the help of Cl^-, NH_4^+ produced in the reaction process was oxidized to N_2 by breakpoint chlorination. The results showed that only 2 g/L NaCl was needed to completely convert NO_3^- to N_2. In addition, Ru-Cu_2O/Co_3O_4@CF also showed superior stability, and after 20 cycles, it still maintained nearly 100% NO_3^- removal rate and N_2 selectivity. This work provides valuable insights for water pollution control and electrochemical denitrification.

2 Materials and methods

2.1 Synthesis of Cu-Co layered double hydroxide (LDH)@CF

The CF (3 cm × 2 cm × 1 mm) was first ultrasonically treated in 1 M HCl, ethanol, and ultrapure water for 15 min each to remove surface oxide layers and oil contaminants. The treated CF was then dried at 60 °C for subsequent use. In a typical synthesis, 272 mg of $Cu(NO_3)_2{\cdot}3H_2O$ and 327 mg of $Co(NO_3)_2{\cdot}6H_2O$ (chemical and reagents were provided in Section S1 in the Electronic Supplementary Material (ESM)) were dissolved in 30 mL of ultrapure water. After stirring for 10 min, 630 mg of $CO(NH_2)_2$ and 50 mg of NH_4F were added to the solution with 10 min of stirring. The pretreated CF and the homogeneous 30 mL above solution were transferred into a 50 mL Teflon-lined autoclave, which was then placed in a stainless-steel autoclave and heated at 100 °C for 4 h. After naturally cooling to room temperature, the resulting product was rinsed three times with ultrapure water to remove loosely adhered materials from the CF surface. The sample was subsequently dried in a vacuum oven at 60 °C for 6 h, yielding the LDH-based Cu-Co LDH@CF electrode. For comparison, a Co-free electrode was also prepared under identical synthesis conditions, except that no $Co(NO_3)_2$ $6H_2O$ was added. This self-supported catalyst was denoted as the Cu LDH@CF electrode.

2.1.1 *Preparation of Ru/Cu-Co LDH@CF electrodes*

200 μL of $RuCl_3{\cdot}xH_2O$ solution (250 mg/mL) was added to 30 mL of ultrapure water and stirred thoroughly to ensure complete mixing. The as-prepared Cu-Co LDH@CF was then immersed in the $RuCl_3$ solution under continuous stirring for 12 h. After the reaction, the sample was retrieved, rinsed three times with ultrapure water, and dried in a vacuum oven at 60 °C for 6 h. The final product was denoted as Ru/Cu-Co LDH@CF.

2.1.2 *Preparation of Ru-Cu_2O/Co_3O_4@CF electrodes*

The dried Ru/Cu-Co LDH@CF was subsequently subjected to annealing in a tube furnace under a nitrogen atmosphere. The temperature (T) was raised to 350 °C at a heating rate of 3 °C/min, maintained for 2 h, and then allowed to cool naturally to room temperature. The final product, denoted as the Ru-Cu_2O/Co_3O_4@CF, was obtained through this process.

2.2 Electrocatalytic test

All electrochemical measurements were performed using a CHI 760E electrochemical workstation. The tests were conducted in a 100 mL single-cell containing 75 mL electrolyte with a standard three-electrode configuration: The working electrode was the as-prepared Ru-Cu_2O/Co_3O_4@CF sample (1 cm × 1.5 cm), the reference electrode was Ag/AgCl (all potentials were converted to the reversible hydrogen electrode (RHE) scale using the equation $E_{RHE} = E_{Ag/AgCl} + 0.059 \times pH + 0.197$, where E_{RHE} was the potential referenced to RHE and $E_{Ag/AgCl}$ was the potential measured versus the Ag/AgCl reference electrode), and a Pt sheet (1 cm × 1 cm)

served as the counter electrode. To systematically investigate the catalytic performance of the Ru-Cu_2O/Co_3O_4@CF electrode, various electrolyte conditions were evaluated: NO_3^- concentration (25, 50, 75, and 100 mg/L NO_3^-–N), chloride ion concentration (0, 1, 2, and 3 g/L), pH (3, 5, 6.69 (initial), 9, and 11), and the pH was adjusted using 0.1 M HCl or 0.1 M NaOH.

Cyclic voltammetry (CV) and linear sweep voltammetry (LSV) were performed at a scan rate of 100 mV/s within a potential window of 0 to −1.61 V (vs. Ag/AgCl). Chronoamperometry experiments were conducted at different applied potentials for 4 h. During electrolysis, 1 mL of the electrolyte was sampled hourly to analyze the concentrations of NO_3^-–N, NO_2^-–N, and NH_4^+–N. To calculate the stability of the catalyst, the Ru-Cu_2O/Co_3O_4@CF was carefully rinsed with deionized water after each test and dried in a vacuum oven at 60 °C for subsequent reuse. The whole reaction process was maintained at 25 °C in a water bath, and the speed of 300 rpm was maintained by magnetic stirring. Before electrolysis, high-purity Ar (99.99 %) was swept through the electrolyte for 30 min to remove dissolved O_2 and N_2, and Ar was also continuously introduced during electrocatalysis.

3 Results and discussion

3.1 Characterizations of electrodes

A self-supported catalytic material based on CF was successfully prepared for the efficient electrochemical reduction of NO_3^- (Fig. 1). Figures 1(b) and 1(c) show low- and high-magnification scanning electron microscopy (SEM) images of the pure CF substrate (material characterization is provided in Section S2 in the ESM). The surface of the original CF was relatively smooth and flat, with some natural fiber textures and grooves, which provided sufficient specific surface area and a good adhesion foundation for the subsequent growth of the catalyst. Figures 1(d) and 1(e) display the microstructure of Cu-Co LDH@CF after hydrothermal synthesis. Compared with pure CF, its surface is covered with a dense and uniform nanosheet array. These nanosheets interlaced and grew vertically, forming an open hierarchical pore structure. This unique three-dimensional nanosheet array structure considerably increases the active specific surface area of the material, which allows electrolyte penetration and reaction mass transfer, and provides abundant active sites for the electrocatalytic reaction. Figures 1(f) and 1(g) demonstrate the morphology of Ru-Cu_2O/Co_3O_4@CF. Abundant small granular substances are successfully loaded on the surface of the original LDH nanosheet framework, which are considered to be Ru-doped Cu/Co oxide composites. The multiphase heterojunction structure is expected to enhance the catalytic activity of the material through interfacial synergy.

Transmission electron microscopy (TEM) measurement was performed to analyze the crystal structure of the material in detail (Figs. 1(h)–1(j)). The low-magnification TEM image (Fig. 1(h)) confirmed its flake-like structure. The high-resolution TEM (HRTEM) images (Figs. 1(i) and 1(j)) showed distinct lattice fringes. The measured lattice spacings of 0.2029 and 0.2277 nm corresponded to the (400) crystal plane of Co_3O_4 and the (200) crystal plane of Cu_2O [7, 29], respectively, demonstrating the successful construction of the Cu_2O–Co_3O_4 heterojunction. In addition, the lattice spacings of 0.1997 and 0.2325 nm corresponded to the (111) crystal plane of metallic Cu and the (100) crystal plane of Ru [7, 12], respectively, which confirmed the *in-situ* growth of Ru nanoparticles on the CF substrate. This indicated that the prepared catalytic material was a metal-oxide composite system rather than a single-phase material. The elemental distribution of Ru-Cu_2O-Co_3O_4@CF was characterized by energy dispersive X-ray spectroscopy (EDS) elemental mapping (Fig. 1(k)). The results indicated that Cu, Co, and O were uniformly distributed within the selected area and coincided with the three-dimensional skeletal morphology of the material, demonstrating the successful loading and uniform distribution of the active components. Ru signal points were visible and evenly dispersed on the Cu and Co support, indicating that the noble metal Ru was efficiently loaded and well dispersed, thereby avoiding severe agglomeration, which is conducive to maximizing its atomic utilization and catalytic efficiency. Table S1 in the ESM (microscopic local relative content from TEM-EDS) shows that Ru has the highest mass percentage (42.82%), yet its atomic percentage (25.18%) is close to that of Cu (23.32%) and Co (25.44%). However, the mass percentage of metals obtained by digestion method is shown in Table S2 in the ESM. It can be seen that the contents of Ru and Co are very small. Combined with the results of TEM-EDS analysis, it shows that Ru and Co are mainly distributed on the surface of CF.

As shown in the X-ray diffraction (XRD) patterns (Fig. 2(a)), the characteristic peaks of the (111) and (200) crystal planes of Cu_2O (PDF#98-000-0186) appear at 36.4° and 42.3°, respectively [16], and distinct diffraction peaks appear at 43.3° and 50.4°, corresponding to the (111) and (200) crystal planes of metallic Cu (PDF#04-004-4642) [32], respectively. Additionally, the strongest diffraction peak of Co_3O_4 was located at 36.8° (PDF#04-006-3982) [33], which was close to the position of the diffraction peak from the (111) crystal plane of Cu_2O. Furthermore, the diffraction peak from the (400) crystal plane occurred at 44.8° [34], a position relatively close to that of the strongest diffraction peak of Cu. The diffraction peak intensity of Cu was higher than that of the other phases, which was directly related to the CF serving as a self-supporting substrate. No obvious diffraction peaks of Ru compounds were observed in the XRD patterns, indicating that Ru may exist in a highly dispersed state, which is consistent with the uniform distribution of Ru in the elemental mapping results.

The binding energy scanning range of the C 1s spectra (Fig. 2(b)) was 275 to 295 eV, which overlapped with that of the Ru 3d spectra. The binding energy peak of the Ru $3d_{5/2}$ orbital was at 280.34 eV, and the binding energy peak of its $3d_{3/2}$ orbital was at 284.68 eV, which highly coincided with the standard binding energy peak of the C–C bond at 284.80 eV [35]. As shown in Fig. 2(f), the Ru 3p orbital of Ru-Cu_2O/Co_3O_4@CF undergoes energy level splitting due to spin-orbit coupling, forming a pair of doublets Ru $3p_{3/2}$ and Ru $3p_{1/2}$, and the energy difference between the two is approximately 22.15 eV, a value that highly coincides with the standard spin-orbit splitting value of Ru^0 (about 22 eV), supporting the existence of metallic Ru [36]. The presence of oxidized Ru would typically shift the binding energy of Ru $3p_{3/2}$ to a higher value (463–465 eV). The absence of a noticeable positive shift in the figure indicates that no considerable oxidation of Ru occurred on the sample surface, suggesting that Ru primarily existed in a metallic state within the sample. This finding is consistent with the TEM and XRD results.

The O 1s spectra (Fig. 2(c)) illustrate the distribution of oxygen species on the catalyst surface. Lattice oxygen (metal–O) was observed at 530 eV [36], indicative of metal–O bonds, such as Cu–O and Co–O. Hydroxyl H–O and adsorbed water indicate the

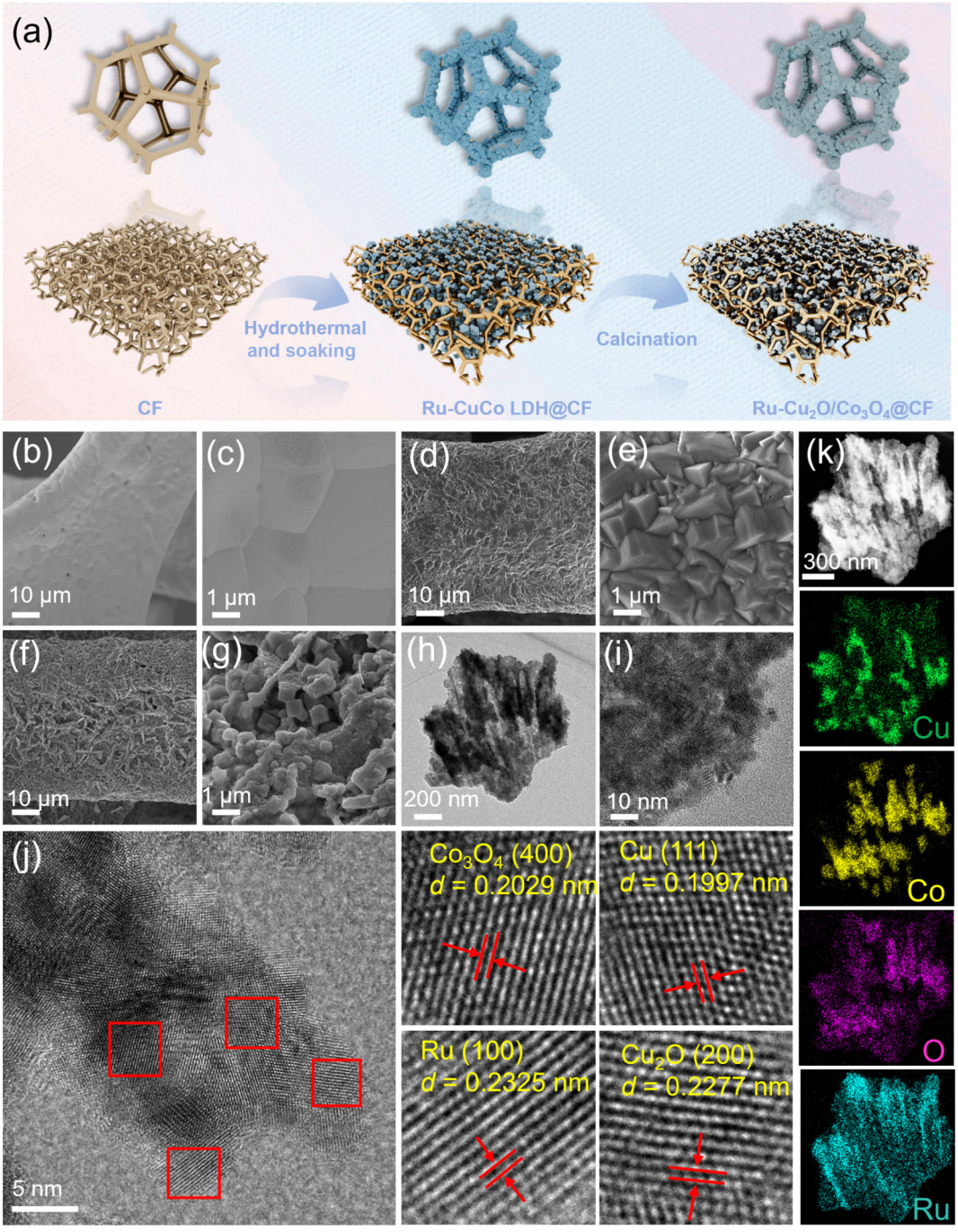

Figure 1 (a) Schematic diagram and the synthesis process of Ru-Cu_2O/Co_3O_4@CF and SEM images of ((b) and (c)) pure CF, ((d) and (e)) Cu-Co LDH@CF, and ((f) and (g)) Ru-Cu_2O/Co_3O_4@CF at different resolutions. ((h)–(j)) TEM images of Ru-Cu_2O/Co_3O_4@CF at different resolutions. (k) EDS elemental mapping of Ru-Cu_2O/Co_3O_4@CF.

presence of hydroxyl groups or physically adsorbed water on the material's surface. The figure illustrates that lattice oxygen is substantially reduced, whereas H–O markedly increases following the introduction of Ru, indicating that the metal oxides on the material surface are considerably decreased. The lattice loses oxygen atoms, resulting in positively charged vacancies known as oxygen vacancies, which can augment the catalyst activity, activate reaction molecules, and reduce the reaction energy barrier.

The peaks at 932.68 and 952.48 eV in Ru-Cu_2O/Co_3O_4@CF (Fig. 2(d)) are ascribed to $Cu^{0/+}$ $2p_{3/2}$ and $Cu^{0/+}$ $2p_{1/2}$, respectively [37], and they are shifted by 0.3 eV (from 932.38 eV) and 0.2 eV (from 953.28 eV) relative to the peaks of Cu-Co LDH@CF, respectively. Additionally, Cu species on the surface of the catalyst were analyzed by Cu LMM, and it was found that the peak of Cu LMM was at 916.5 eV (Fig. S4 in the ESM), indicating that Cu^+ was dominant on the surface of the catalyst. In addition, Ru-Cu_2O/Co_3O_4@CF and Cu-Co LDH@CF exhibit characteristic peaks for Co^{3+} $2p_{1/2}$ and Co^{3+} $2p_{3/2}$ at 796.33, 780.07, 796.42, and 780.79 eV [38], respectively (Fig. 2(e)). It shows that electron transfer has taken place at the heterogeneous interface in Ru-Cu_2O/Co_3O_4@CF, which further

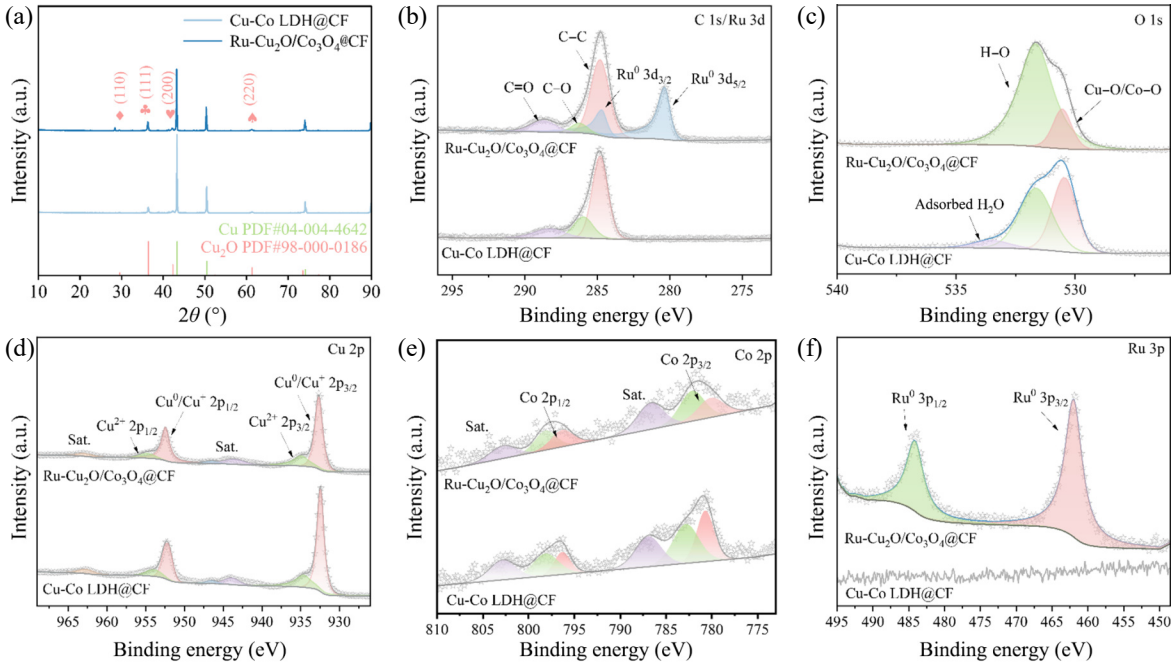

Figure 2 (a) XRD patterns of Cu-Co LDH@CF and Ru-Cu_2O/Co_3O_4@CF. ((b)–(f)) X-ray photoelectron spectroscopy (XPS) spectra of Ru-Cu_2O/Co_3O_4@CF.

proves the successful synthesis of heterostructure.

3.2 Performance comparison of different catalysts

Figure 3 shows the performance comparison of different catalysts in the electrochemical NO_3^- reduction reaction. In the concentration time curves in Figs. 3(a)–3(e), Ru-Cu_2O/Co_3O_4@CF exhibits the best NO_3^- removal efficiency (the methods for detecting N-containing species are described in Section S3 in the ESM). The removal rate of NO_3^-–N reaches as high as 98.44% within 4 h, and N_2 selectivity is approximately 100% (the calculation method is provided in Section S4 in the ESM). Additionally, although the NO_3^-–N removal performance of Ru/Cu-Co LDH@CF is good, reaching around 97%, and its N_2 selectivity is 100% in the first working cycle, it considerably declines to 73.79% and 66.64% in the second and third working cycles, respectively (Fig. S5 in the ESM). This indicates that Ru/Cu-Co LDH@CF without tube furnace annealing has poor stability, and the loaded Ru may become ineffective or leach into the electrolyte after one experiment. Cu LDH@CF and Cu-Co LDH@CF exhibited considerable NO_2^- accumulation, whereas Ru/Cu-Co LDH@CF and Ru-Cu_2O/Co_3O_4@CF catalysts demonstrated lower intermediate (NO_2^-–N and NH_4^+–N) accumulation, indicating that Ru doping effectively minimizes the formation of intermediates during NO_3^- reduction. This is attributed to the introduction of Ru, which may provide more active sites and highly active hydrogen species, promoting the further reduction of key intermediates and effectively suppressing the generation of NO_2^-. The Ru-Cu_2O/Co_3O_4@CF catalyst shows the best comprehensive performance in the NO_3^- reduction reaction, with a high removal rate and high N_2 selectivity, making it the most promising catalyst material for practical application.

3.3 Influence of $RuCl_3$ contents

Figure 4 shows an analysis of the influence of doping with different $RuCl_3$ contents on the catalytic performance of the self-supporting composite material Ru-Cu_2O/Co_3O_4@CF during material synthesis. As the $RuCl_3$ dosage increases from 0 to 200 μL (250 mg/L), the NO_3^-–N removal rate and N_2 selectivity show a considerable upward trend. This may be because the introduction of Ru species optimizes the electron transfer pathway, plays a crucial role in promoting the formation of the N≡N bond, and facilitates the directional conversion of $NO_3^- \rightarrow NO_2^- \rightarrow N_2$. When the content reaches 200 μL, the catalytic system achieves a NO_3^-–N removal rate of 98.44% within 4 h, with approximately 100% N_2 selectivity. Compared to the sample without $RuCl_3$ doping, the removal rate increases by approximately 45% (from 53.22%), and N_2 selectivity increases by approximately 33% (from 62.85%). However, when the content is further increased to 400 μL, the removal rate is 98.18%, and N_2 selectivity is approximately 100%. This indicates that there is an optimal doping threshold for the $RuCl_3$ content. Excessive Ru may lead to the overaggregation of active sites, resulting in a decrease in the specific surface area. In addition, it may trigger a competitive hydrogen evolution reaction. Therefore, considering the usage amount and cost of noble metals, 200 μL of $RuCl_3$ was doped for material synthesis in subsequent experiments.

3.4 Influence of applied potentials

This study analyses the influence of different applied potentials (−1.21, −1.41, −1.61, and −1.81 V vs. Ag/AgCl) on the electrochemical NO_3^- reduction performance of Ru-Cu_2O/Co_3O_4@CF. Figures 5(a)–5(d) show that the more negative the applied potential, the faster the decrease rate of the NO_3^-–N concentration, indicating a considerable enhancement of the reduction reaction kinetics. As the potential decreases from −1.21 to −1.81 V, the catalytic activity of the electrode shows a gradient increase. At −1.21 V, the removal of NO_3^-–N is relatively slow, and a high residual concentration remains after 4 h of reaction. At −1.81 V, NO_3^-–N is nearly completely removed within 4 h, indicating that a strongly negative potential considerably improves the mass transfer process and electron transfer efficiency. No considerable accumulation of intermediate products NO_2^-–N and NH_4^+–N at all potentials was observed, demonstrating that Ru-

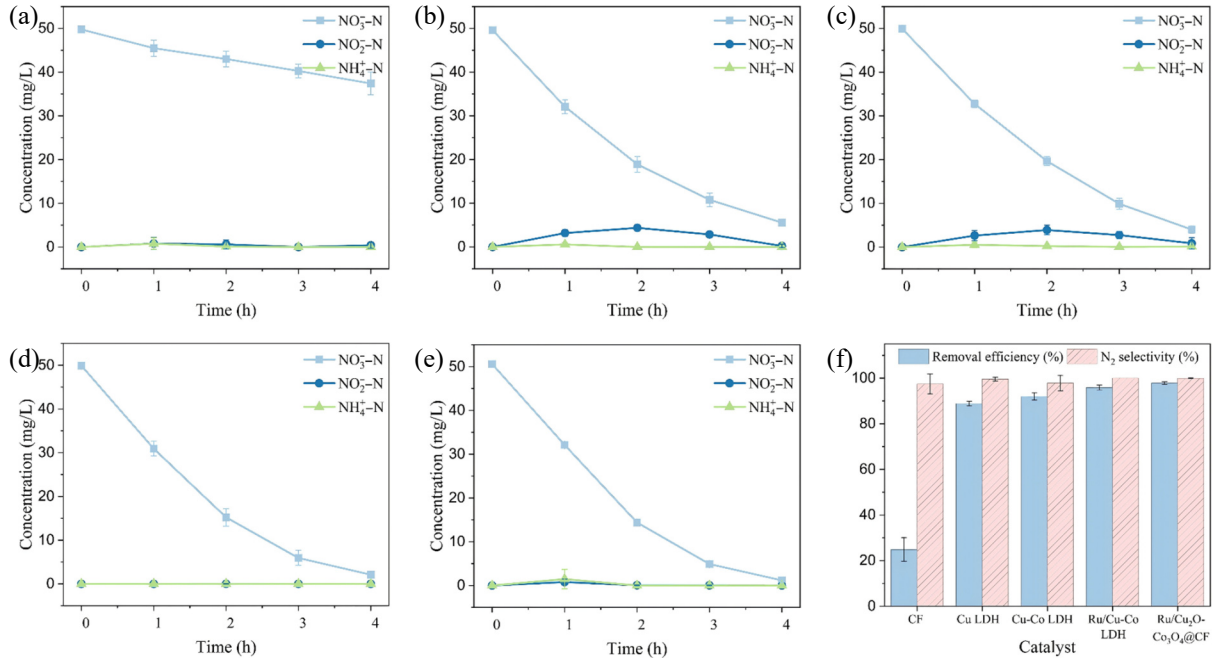

Figure 3 ((a)–(e)) Concentrations of NO_3^-–N, NO_2^-–N, and NH_4^+–N when using different catalysts (CF, Cu LDH, Cu-Co LDH, Ru/Cu-Co LDH, and Ru-Cu_2O/Co_3O_4@CF). (f) NO_3^-–N removal efficiency and N_2 selectivity for different catalysts (experiment conditions: T = 25 °C, pH = 6.50, 50 mg/L NO_3^-–N, 3 g/L NaCl, and $E_{Ag/AgCl}$ = −1.61 V vs. Ag/AgCl).

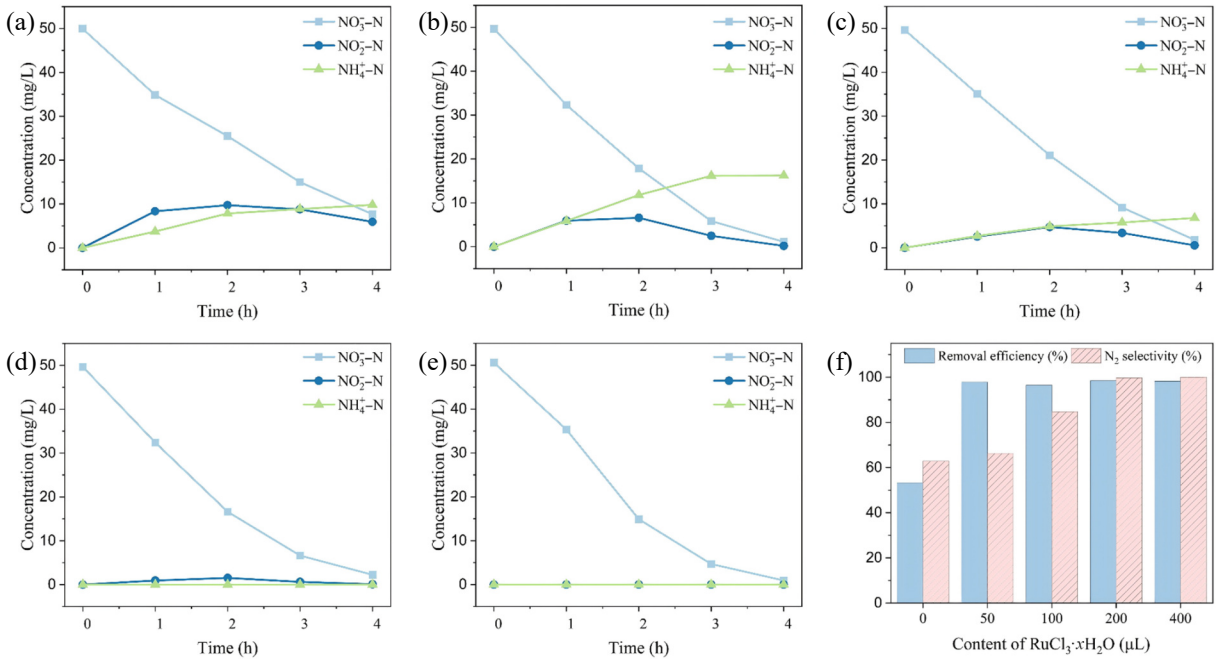

Figure 4 ((a)–(e)) Concentrations of NO_3^-–N, NO_2^-–N, and NH_4^+–N when using different contents of $RuCl_3$ (0, 50, 100, 200, and 400 μL). (f) NO_3^-–N removal efficiency and N_2 selectivity for different contents of $RuCl_3$.

Cu_2O/Co_3O_4@CF has excellent reaction pathway regulation ability and can inhibit the generation of NO_2^- and NH_4^+.

Figure 5(e) shows the changes in the percentage content of each component over time at an applied potential of −1.61 V vs. Ag/AgCl. This indicates that during the entire reduction process, the Ru-Cu_2O/Co_3O_4@CF electrocatalyst converts most of the NO_3^-–N into N_2, and the instantaneous concentration percentages of NO_2^-–N and NH_4^+–N are small, demonstrating the excellent N_2 selectivity of the self-supporting electrocatalyst. In addition, Fig. 5(f) shows that N_2 selectivity remains at a high level at all potentials, indicating good intrinsic selectivity of the catalyst. Thermodynamically, the increase in negative potential enhances the cathodic reduction driving force, making the Gibbs free energy of NO_3^- reduction more negative. Kinetically, as the potential decreases from −1.21 to −1.81 V, the reaction rate constant increases. The voltage range of −1.61 to −1.81 V (vs. Ag/AgCl) represents the optimal operating window for the catalytic reaction. To balance energy utilization efficiency, this study selected −1.61 V as the applied potential for subsequent experiments.

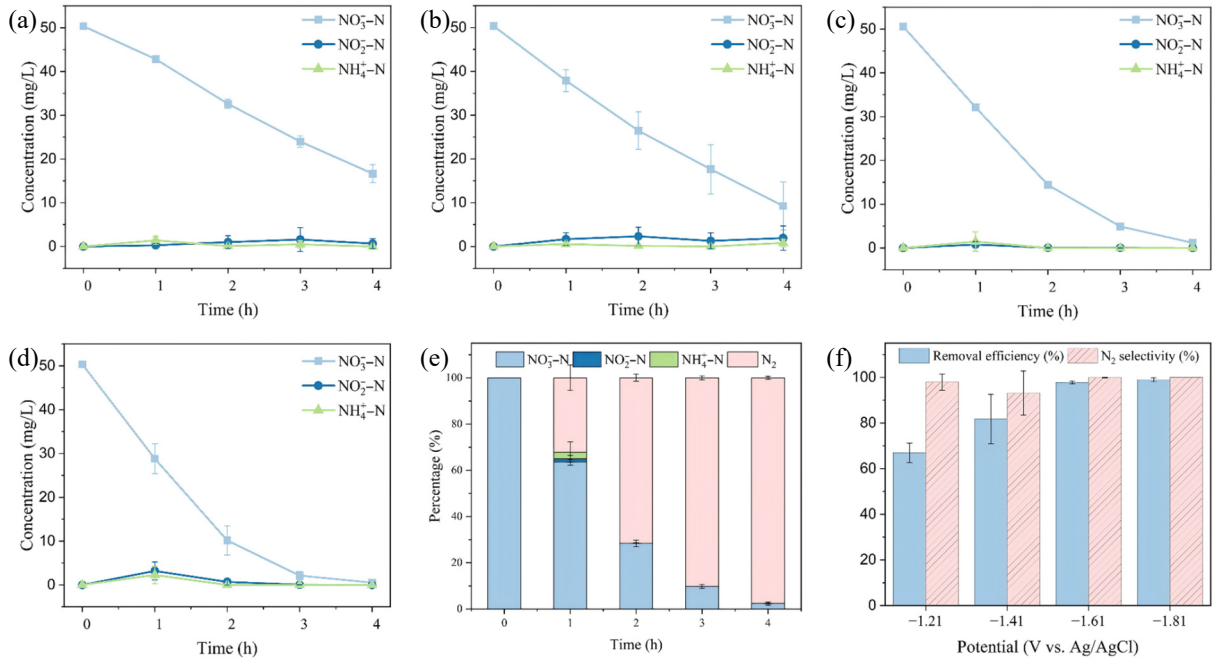

Figure 5 ((a)–(d)) Concentrations of NO_3^-–N, NO_2^-–N, and NH_4^+–N at different current densities −1.21, −1.41, −1.61, and −1.81 V vs. Ag/AgCl). (e) Variation in the concentration percentages of NO_3^-–N, NO_2^-–N, NH_4^+–N, and N_2 over time at a potential of −1.61 V vs. Ag/AgCl. (f) NO_3^-–N removal efficiency and N_2 selectivity for different potentials.

3.5 Influence of Cl^- concentrations

Figure 6 shows the influence of different NaCl concentrations (0, 1, 2, and 3 g/L) in the electrolyte on the electrochemical NO_3^- reduction performance of Ru-Cu_2O/Co_3O_4@CF. Figures 6(a)–6(d) show the trends of the concentrations of NO_3^-–N, NO_2^-–N, and NH_4^+–N over time under the four NaCl concentration conditions. Chlorine ion undergoes electro-oxidation reaction on the anode surface, losing electrons to generate chlorine gas, which is rapidly hydrolyzed in acidic aqueous solution to generate strong oxidizing hypochlorous acid (Eqs. (1) and (2)). Hypochloric acid transforms NH_4^+ into N_2 through oxidation, thus realizing complete denitrification (Eq. (3)). Under all NaCl concentration conditions, NO_3^-–N concentrations exhibited a considerable downward trend, indicating that NO_3^- concentration changes are unaffected by NaCl. The pseudo-first-order kinetic curves (Fig. 6(e)) show a good linear fit under all conditions, confirming that the reaction follows pseudo-first-order kinetics. Except when no NaCl is added, the reaction rate constant k is highest at a NaCl concentration of 3 g/L. This indicates that an appropriate Cl^- concentration may enhance the ionic conductivity and reduce Ohmic losses, thereby improving the conductivity of the electrolyte. Additionally, it can regulate the double-layer structure to optimize the electron transfer process and enhance electron transfer efficiency. However, excessive Cl^- concentration may lead to high ionic strength, suppressing the accessibility of catalyst active sites, or it may react with the reduction products generated by electrochemical NO_3^- reduction, thus reducing the NO_3^-–N removal rate. Figure 6(f) shows that, compared with the case without adding NaCl, the decreased NO_3^-–N removal performance at other NaCl concentrations may be related to diffusion limitation or the surface shielding effect of the catalyst under high ionic strength. In summary, Cl^- can regulate the surface charge distribution of the catalyst through adsorption, optimize the adsorption and activation process of NO_3^-, or inhibit the side reaction of hydrogen evolution, thereby improving the reduction selectivity and rate. The addition of NaCl to the electrolyte considerably regulates the catalytic performance of Ru-Cu_2O/Co_3O_4@CF. Among the concentrations, 3 g/L is optimal, with a high reaction rate (the largest k value), high NO_3^- removal rate (98.44%), and a high N_2 selectivity (100%). Therefore, a NaCl concentration of 3 g/L was used in the other experiments

$$2Cl^- \rightarrow Cl_2 + 2e^- \quad (1)$$

$$Cl_2 + H_2O \leftrightarrow HOCl + Cl^- + H^+ \quad (2)$$

$$HOCl + 2NH_2OH \rightarrow N_2 + Cl^- + 3H_2O + H^+ \quad (3)$$

$$3HOCl + 2NH_4^+ \rightarrow N_2 + 3H_2O + 2H^+ + 3HCl \quad (4)$$

3.6 Influence of initial NO_3^-–N concentrations

Figure 7 shows the catalytic performance of Ru-Cu_2O/Co_3O_4@CF under different initial NO_3^-–N concentrations. Figures 7(a)–7(d) indicate that the rate of NO_3^-–N concentration decreases considerably with increasing initial concentration, demonstrating the high activity of the Ru-Cu_2O/Co_3O_4@CF catalyst for the reduction of low-concentration NO_3^-. As the initial concentration increases, the slope of the pseudo-first-order kinetic curve decreases (Fig. 7(e)), suggesting that the reaction rate decreases with increasing initial concentration. This may be because of the limited number of active sites, which cannot efficiently catalyze reactions at higher substrate concentrations. The generation of by-products increases with increasing initial concentration (Fig. 7(f)). The high initial concentration of NO_3^-–N leads to incomplete reduction of NO_3^-. When the initial NO_3^- concentration is excessively high (75 and 100 mg/L), NO_3^- cannot be completely removed within 4 h. However, if the reaction time of the electrochemical NO_3^- reduction experiment is extended, high NO_3^-–N removal rates and N_2

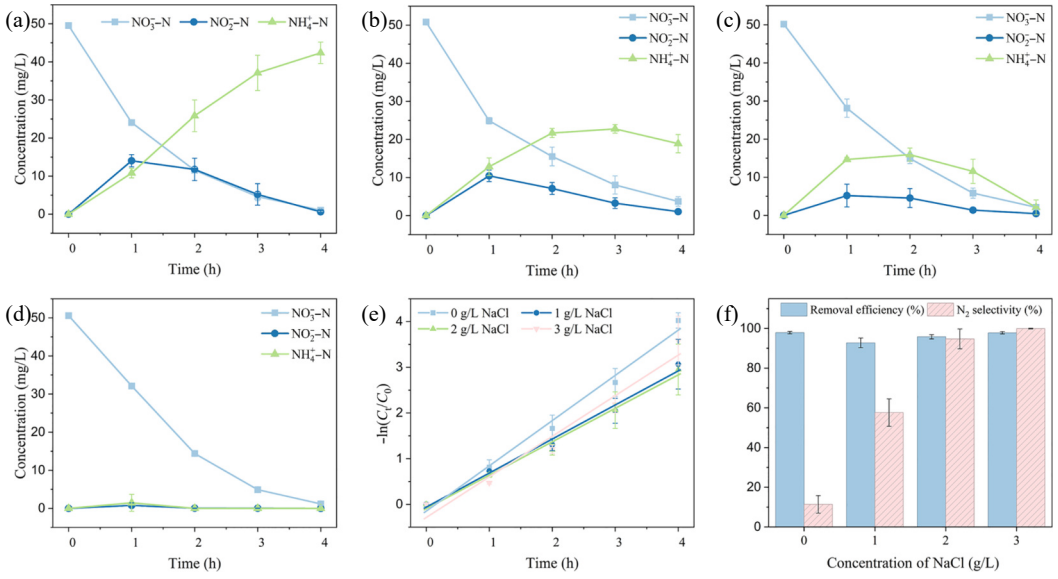

Figure 6 ((a)–(d)) Concentrations of NO_3^-–N, NO_2^-–N, and NH_4^+–N at different concentrations of NaCl (0, 1, 2, and 3 g/L). (e) Pseudo-primary kinetic curves of NO_3^- reduction for different concentrations of NaCl. (f) NO_3^-–N removal efficiency and N_2 selectivity for different concentrations of NaCl.

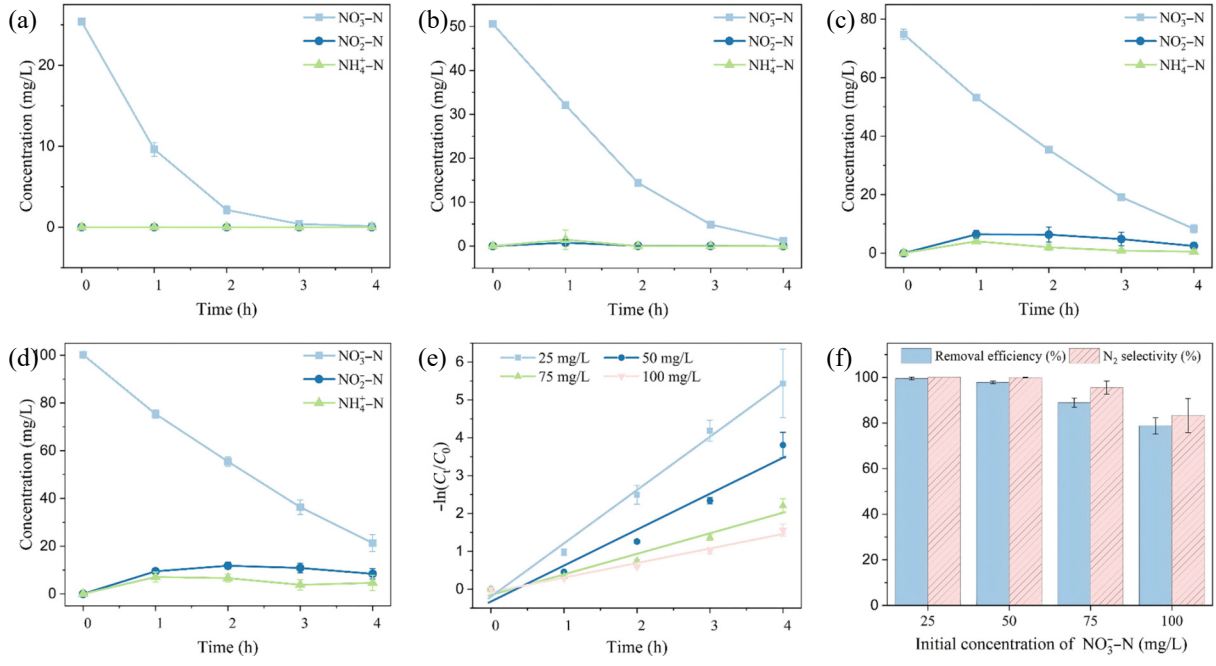

Figure 7 ((a)–(d)) Concentrations of NO_3^-–N, NO_2^-–N, and NH_4^+–N at different concentrations of initial NO_3^-–N (25, 50, 75, and 100 mg/L). (e) Pseudo-primary kinetic curves of NO_3^- reduction for different concentrations of initial NO_3^-–N. (f) NO_3^-–N removal efficiency and N_2 selectivity for different concentrations of initial NO_3^-–N.

selectivity can be achieved at these two initial concentrations over a wide concentration range. Its multicomponent synergy enables it to adapt to different concentrations. Thus, this catalyst is suitable for treating NO_3^- containing wastewater over a wide concentration range; however, operating parameters, such as reaction time and pH, need to be optimized to maintain high N_2 selectivity at high concentrations.

3.7 Influence of electrolyte pH

To investigate the adaptability of the catalyst to environmental pH, the effects of electrolyte pH (3, 5, 6.5, 9, and 11) on the electrochemical NO_3^- reduction reaction performance were explored (Fig. 8). Under all pH conditions, the Ru-Cu_2O/Co_3O_4@CF catalyst exhibited high NO_3^-–N removal rates and N_2 selectivity. However, in acidic environments (pH = 3 and 5), metallic Ru exhibits strong hydrogen evolution performance. It may promote electrochemical NO_3^- reduction through the adsorption of atomic hydrogen, thus not generating other by-products and considerably increasing N_2 selectivity. When the pH is between 9 and 11, the high concentration of OH^- competes with H^+ for active sites, inhibiting important steps that involve protons, such as the hydrogenation of NO_2^-. Moreover, the change in the surface charge of the catalyst under alkaline conditions affects the adsorption of reactants and the efficiency of electron transfer. This causes considerable NO_2^- build-up during the reaction and slows down the rate of the electrochemical NO_3^- reduction process. In

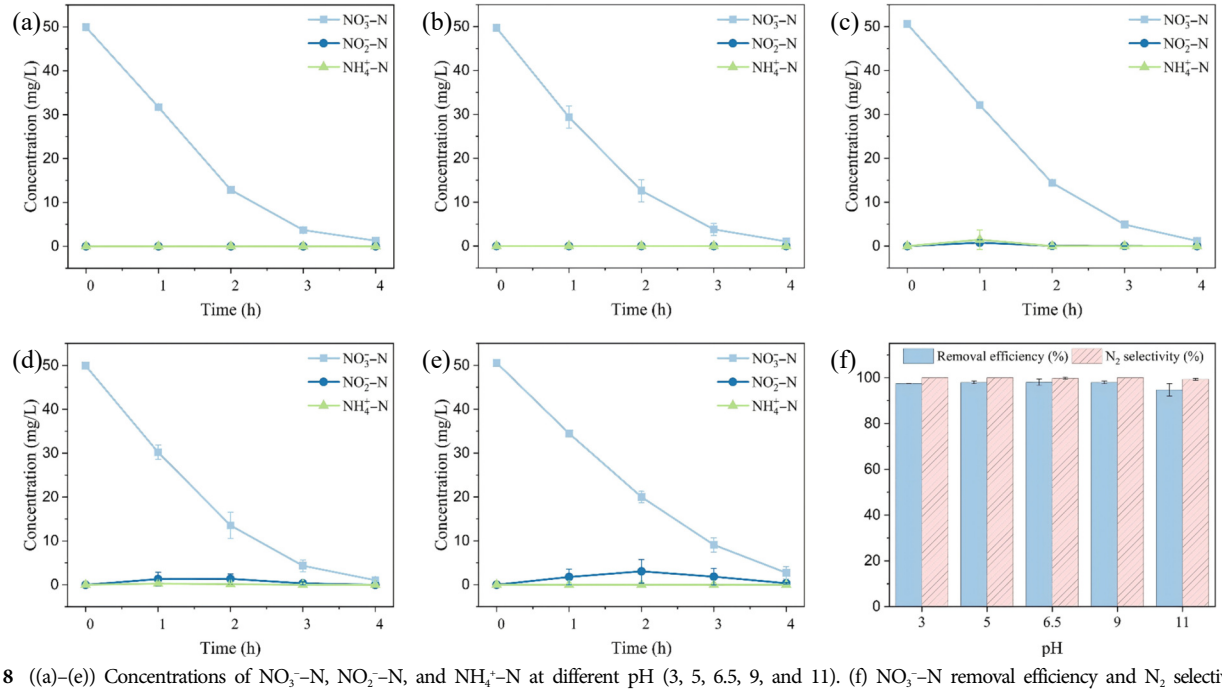

Figure 8 ((a)–(e)) Concentrations of NO_3^-–N, NO_2^-–N, and NH_4^+–N at different pH (3, 5, 6.5, 9, and 11). (f) NO_3^-–N removal efficiency and N_2 selectivity for different pH.

actual wastewater treatment, most wastewater is near neutral, and the Cu_2O/Co_3O_4@CF catalyst is highly effective at converting NO_3^- to N_2 under near-neutral conditions.

3.8 Mechanism of NO_3^- reduction and stability

The mechanism diagram of NO_3^- reduction to N_2 is shown in Fig. 9(a). In an electrocatalytic system without NaCl, NO_3^- is reduced to NH_4^+ at the cathode through a series of multi-step electron transfer and proton-coupled reactions. NO_3^- first adsorbs onto Ru-Cu_2O/Co_3O_4@CF surface and undergoes multiple reductions to form key nitrogen-containing intermediates, such as $*NO_3$ and $*NO_2$. This is followed by continuous hydrogenation reactions, sequentially forming hydrogenated intermediates like *NOH, *NH, and $*NH_2$. Finally, an 8-electron transfer is completed to produce NH_4^+, which then desorbs from the surface (as shown in Eqs. (5)–(13)). *In-situ* attenuated total reflectance Fourier transform infrared (ATR-FTIR) spectroscopy was used to reveal the surface-adsorbed intermediates. As shown in Fig. 9(b), in the electrocatalytic system without NaCl, the characteristic peaks at approximately 1550, 1500, and 1280 cm^{-1} correspond to the *NOH, $*NH_2$, and *NH species, respectively [39, 40], providing strong evidence that NO_3^- is reduced to NH_4^+ in the absence of Cl^-, which is consistent with the experimental results (Fig. 6(a)). After adding NaCl to the electrolyte solution, on one hand, Cl^- can adsorb onto the active sites of the catalyst, modulating the adsorption strength of intermediates, promoting the coupling of two intermediates, such as NO or *NOH, to form a dinitrogen intermediate, which is then converted to N_2O through deoxygenation and hydrogenation, and finally reduced to N_2. On the other hand, Cl^- can be oxidized on the electrode surface to form active chlorine species, further oxidizing and coupling the NH_4^+ generated during the reduction process into N_2 (as shown in Eqs. (1)–(4)) [41, 42]. At the same time, the *in-situ* infrared spectra after adding Cl^- also support this theory, with the peaks of *NOH, $*NH_2$, and *NH species significantly weakening (Fig. 9(c)), indicating that the activation kinetics of these intermediates on the catalyst surface are accelerated, rapidly converting them into N_2

$$NO_3^- \rightarrow *NO_3^- \quad (5)$$

$$*NO_3 + H_2O + e^- \rightarrow *NO_2 + 2OH^- \quad (6)$$

$$*NO_2 + H_2O + e^- \rightarrow *NO + 2OH^- \quad (7)$$

$$*NO + H^+ + e^- \rightarrow *NOH \quad (8)$$

$$*NOH + H^+ + e^- \rightarrow *NHOH \quad (9)$$

$$*NHOH + H^+ + e^- \rightarrow *NH + H_2O \quad (10)$$

$$*NH + H^+ + e^- \rightarrow *NH_2 \quad (11)$$

$$*NH_2 + H^+ + e^- \rightarrow *NH_3 \quad (12)$$

$$*NH_3 \rightarrow NH_3 \quad (13)$$

Figure 9(d) shows the results of the catalytic performance stability test for the Ru-Cu_2O/Co_3O_4@CF electrode over 20 cycles (80 h) of operation. The results indicate that the catalyst was highly efficient and stable. Throughout the 20 cycles, the NO_3^-–N removal rate remained consistently high within the range of 94.19% to 99.53%, with a minimal fluctuation range (approximately 5%). N_2 selectivity was stable between 93.62% and 100%, which was highly consistent with the trend of the removal rate. This suggests that the electrode rarely produces by-products (such as NO_2^- or NH_4^+) during NO_3^- reduction, and the main product is environmentally friendly N_2. These results demonstrate the excellent stability of the catalytic activity of the electrode during long-term operation. Compared with many electrodes reported in the references (shown

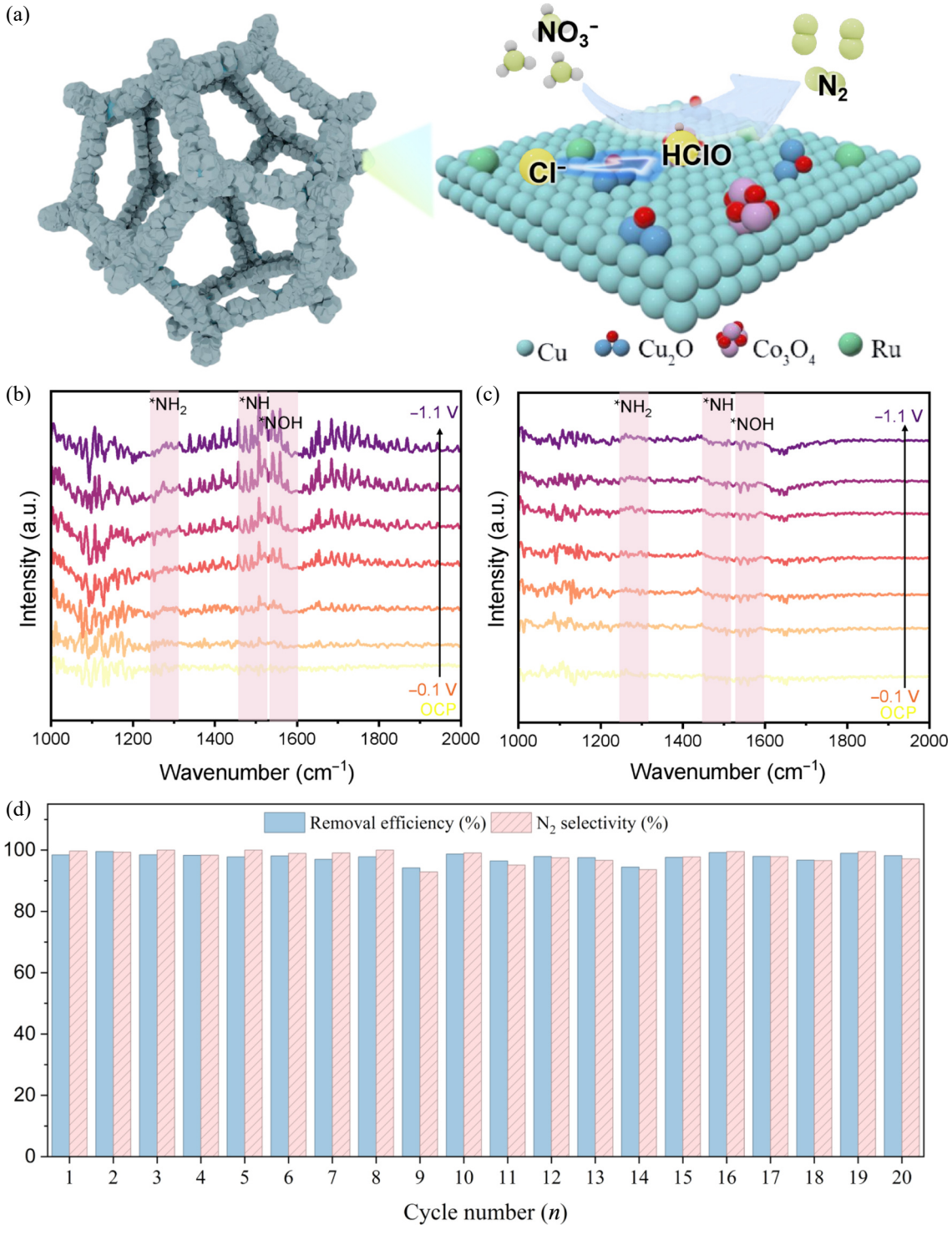

Figure 9 (a) Mechanism diagram and ((b) and (c)) the *in-situ* FTIR spectra of electrocatalytic reduction of NO_3^-: (b) without NaCl and (c) with 2 g/L NaCl. (d) NO_3^-–N removal efficiency and N_2 selectivity of Ru-Cu_2O/Co_3O_4@CF over 20 cycles of reuse.

in Table S3 in the ESM), this electrode maintained approximately 100% removal rate and selectivity after 20 cycles, with an extremely low performance decay rate, considerably outperforming most catalysts [43–54]. The stability test data of this study support the feasibility of long-term use of this electrode in practical wastewater treatment.

4 Conclusions

In this study, a hierarchical-structured catalyst, Ru-Cu_2O/Co_3O_4@CF, was successfully prepared via hydrothermal synthesis, impregnation, and tube-furnace annealing operations. The catalyst uses CF as a self-supporting substrate, is supported by Cu-Co LDH nanosheet arrays, and is loaded with Ru-modified nanoparticles. The composition and chemical valence states of its active

components were verified using conventional characterization and analysis techniques. Additionally, the catalytic performance under different conditions was investigated using electrochemical NO_3^- reduction tests. Ru-Cu_2O/Co_3O_4@CF exhibits excellent NO_3^- catalytic performance. At an applied potential of −1.61 V vs. Ag/AgCl in an electrolyte containing 3 g/L of NaCl, 50 mg/L of NO_3^-–N can be rapidly converted into clean and green N_2 within 4 h. The NO_3^-–N removal rate reaches 98.44%, and the N_2 selectivity is close to 100%, enabling efficient NO_3^- removal and green N_2 conversion. The Ru-Cu_2O/Co_3O_4@CF electrode has an excellent intermediate product control ability, avoiding the accumulation of harmful by-products, thereby preventing secondary pollution and meeting environmental protection requirements. The Ru-Cu_2O/Co_3O_4@CF electrode demonstrates outstanding catalytic stability and selectivity during long-term cycling, with high NO_3^- removal rates and N_2 generation efficiency. Therefore, it is a highly promising electrocatalytic material. This study provides an important reference for electrode design and process optimization of electrochemical NO_3^- reduction technology.

Electronic Supplementary Material: Supplementary material (further details of materials and reagents, material characterization, detection methods, etc.) is available in the online version of this article at https://doi.org/10.26599/NR.2026.94908836.

Data availability

All data needed to support the conclusions in the paper are presented in the manuscript and the Electronic Supplementary Material. Additional data related to this paper may be requested from the corresponding author upon request.

Acknowledgements

This work was supported by Yunnan Provincial Science and Technology Project at Southwest United Graduate School (No. 202502AQ080002), the National Natural Science Foundation of China (No. 22476170), the Science and Technological Talents and Platform Plan Project of Yunnan Province (No. 202505AW340011), and Double-First Class University Plan, the Practical Innovation Project of Postgraduate Students in the Professional Degree of Yunnan University (No. ZC-252511742).

Declaration of competing interest

All the contributing authors report no conflict of interests in this work.

Author contribution statement

J. H.: Investigation, data curation, validation, writing manuscript, experimental design. J. Z. and M. L. Z.: Investigation, data curation, project administration, validation, experimental design. Y. H., X. G. A., and D. F.: Project administration, final analysis, validation. G. Z. H.: Project administration, funding acquisition, writing manuscript. All the authors have approved the final manuscript.

Use of AI statement

None.

References

[1] Yao, X. H.; Li, W.; Cui, D. X.; Dong, M.; Shan, G. G.; Zhang, M.; Wang, X. L.; Su, Z. M.; Sun, C. Y. Dual-metal sites in MOF synergistic boosting NH_3 production under low-nitrate concentration. *Nano Res.* **2025**, *18*, 94907592.

[2] Zhou, J.; Gao, S. S.; Hu, G. Z. Recent progress and perspectives on transition metal-based electrocatalysts for efficient nitrate reduction. *Energy Fuels* **2024**, *38*, 6701–6722.

[3] Liu, Z. X.; Shen, F.; Shi, L.; Tong, Q. W.; Tang, M. E.; Li, Y. M.; Peng, M.; Jiao, Z. J.; Jiang, Y.; Ao, L. et al. Electronic structure optimization and proton-transfer enhancement on titanium oxide-supported copper nanoparticles for enhanced nitrogen recycling from nitrate-contaminated water. *Environ. Sci. Technol.* **2023**, *57*, 10117–10126.

[4] Feng, Z. X.; He, Y. X.; Cui, Y. H.; Qu, Y. B.; Ding, G. P.; Chen, X.; Sui, C. Y.; Wei, Q. L.; Wang, Z. L.; Jiang, Q. Efficient tandem electrocatalytic nitrate reduction to ammonia on bimodal nanoporous Ag/Ag–Co across broad nitrate concentrations. *Nano Lett.* **2024**, *24*, 11929–11936.

[5] Rao, T. Q.; Chen, Y. T.; Hong, Y. H.; Yu, F. S.; Zhang, L. H. Boosting electrochemical nitrate reduction over a wide concentration range through constructing bidirectional electron transfer channels. *ACS Appl. Mater. Interfaces* **2025**, *17*, 37918–37926.

[6] Wang, Z. C.; Liu, S. S.; Wang, M. F.; Zhang, L. F.; Jiang, Y. Z.; Qian, T.; Xiong, J.; Yang, C. T.; Yan, C. L. *In situ* construction of metal–organic frameworks as smart channels for the effective electrocatalytic reduction of nitrate at ultralow concentrations to ammonia. *ACS Catal.* **2023**, *13*, 9125–9135.

[7] Yu, J. C.; Xi, Z. C.; Su, J. H.; Li, L.; Jing, P.; Xu, X.; Liu, B. C.; Zhang, J. A Cu–Co_3O_4 tandem catalyst for efficient electrocatalytic nitrate reduction at low concentration. *ACS Mater. Lett.* **2024**, *6*, 2591–2598.

[8] Xie, F. T.; Kang, X. X.; Wu, Z. Y.; Zhu, H. L.; Gu, L.; Duan, X. M.; Yang, J. P. Built-in electric field boosted tandem catalysis for rapid electrochemical nitrate reduction to nitrogen. *ACS Nano* **2025**, *19*, 26217–26228.

[9] Wang, X. X.; Winter, L. R.; Wu, X. H.; Fan, Y. Z.; Zhao, Y. M.; Kim, J. H.; Elimelech, M. Intensified atomic utilization efficiency of single-atom catalysts for nitrate conversion via electrified nanoporous membrane. *Sci. Adv.* **2025**, *11*, eads6943.

[10] Huang, T. C.; Liang, T. Y.; You, J.; Huo, Q. H.; Qi, S.; Wan, D.; Shang, C. Y.; Yu, J. Y.; Yang, H. P.; Zhang, X. et al. Single-nickel-atom-stabilized positively charged sub-nanometric ruthenium clusters for efficient reduction of low-concentration nitrate to ammonia. *Adv. Funct. Mater.* **2026**, *36*, e29586.

[11] Sun, W. J.; Ji, H. Q.; Li, L. X.; Zhang, H. Y.; Wang, Z. K.; He, J. H.; Lu, J. M. Built-in electric field triggered interfacial accumulation effect for efficient nitrate removal at ultra-low concentration and electroreduction to ammonia. *Angew. Chem., Int. Ed.* **2021**, *60*, 22933–22939.

[12] Bi, Z. H.; Hu, J.; Xu, M.; Zhang, H.; Zhou, Y. T.; Hu, G. Z. Nitrogen-bridged Fe–Cu atomic pair sites for efficient electrochemical ammonia production and electricity generation with Zn–NO_2 batteries. *Angew. Chem., Int. Ed.* **2024**, *63*, e202313434.

[13] Ge, Y.; Sun, L. Z.; Xu, X. B.; Fu, C. C.; Yin, Z. L.; Zhou, Q.; Shi, P.; Yang, W. B.; Liu, B. Charge-spin-orbit modulated carbon-encapsulated FeP/Fe_3O_4 heterojunctions for ultrafast and stable conversion of low-concentration nitrate to ammonia. *Angew. Chem., Int. Ed.* **2026**, *65*, e19571.

[14] Wang, K.; Chen, Y.; Zhao, T.; Ho, S. H. Breaking dilution limits: Electrocatalytic ammonia production from low-concentration nitrate streams. *Adv. Mater.* **2026**, *38*, e17391.

[15] Gao, W. Q.; Sun, J.; Zhao, G. H. Pd clusters loaded with multivalent Cu foam for superior electrochemical nitrate reduction and selective

N≡N bond formation. *Small* **2024**, *20*, 2310597.
[16] Chen, X. H.; Din, S. T. U.; Li, Y.; Li, W. H.; Niu, W. Z.; Wang, M.; Xie, Y. F.; Sun, H. R.; He, S. S.; Zhou, J. Unveiling the *in situ* dissolution and reconstruction of CoMo for electrocatalytic nitrate reduction to ammonia. *Small* **2026**, *22*, e10560.
[17] Liang, M. X.; He, M. Y.; Ren, J. R.; Shi, Y. T.; Zeng, Y. J.; Lin, Z. Q.; Deng, L. B. Dual-coordinated Cu(I) sites immobilized on $Ti_3C_2T_x$ MXene for efficient conversion of low-concentration nitrate toward ammonia. *Adv. Funct. Mater.* **2026**, *36*, e14022.
[18] Yue, M. Y.; Liu, Y. F.; Cao, Y. H.; Jiang, Y. R.; Dong, K. Z.; Yuan, Q. H.; Wang, Y. J. A Cu_2O-Pd dual active sites tandem catalyst enables efficient nitrate reduction to ammonia at low concentration. *Rare Met.* **2025**, *44*, 5452–5461.
[19] Yang, W. H.; Chang, Z. W.; Yu, X.; Wu, P.; Shen, R. X.; Wang, L. Z.; Cui, X. Z.; Shi, J. L. Cu–Co dual sites tandem synergistic effect boosting neutral low concentration nitrate electroreduction to ammonia. *Adv. Sci.* **2025**, *12*, 2416386.
[20] Hu, J.; Tang, C.; Bi, Z. H.; Zhou, S. X.; Kong, Q. Q.; Gao, S. S.; Liu, X. J.; Zhao, X.; Hu, G. Z. Self-supported iron-doped cobalt–copper oxide heterostructures for efficient electrocatalytic denitrification. *J. Colloid Interface Sci.* **2024**, *675*, 313–325.
[21] Zhao, T. T.; Zhou, J.; Zhang, D. F.; Wang, Y.; Zhou, S. X.; Chen, J. B.; Hu, G. Z. Self-supported P-doped $NiFe_2O_4$ micro-sheet arrays for the efficient conversion of nitrite to ammonia. *J. Colloid Interface Sci.* **2023**, *650*, 143–150.
[22] Wang, X. Y.; Wang, D.; Ma, H. C.; Wang, G. W. Enhancement of ammonia synthesis via electrocatalytic reduction of low-concentration nitrate using co-doped MIL-101(Fe) nanostructured catalysts. *J. Colloid Interface Sci.* **2025**, *677*, 369–377.
[23] Wang, F. T.; Xie, Q. Y.; Jiao, H.; Xu, L. 2D copper metal–organic framework as an electrocatalyst for the highly efficient electrochemical reduction of low concentration nitrate/nitrite-to-ammonia. *J. Solid State Chem.* **2026**, *353*, 125623.
[24] Zhang, M. M.; Lai, C.; Li, B. S.; Xu, F. H.; Hu, X. R.; Ma, D. S.; Tang, L. Synergistic effect of cobalt iron layered double hydroxides with adjacent copper atoms regulates intermediate adsorption and H_2O dissociation to boost electrocatalytic nitrate reduction at ultralow concentrations. *Appl. Catal. B: Environ. Energy* **2025**, *378*, 125599.
[25] Li, Z.; Luo, J.; Yao, L.; Gan, Y. H.; Wang, Z.; Zheng, H. C.; Cai, M. H.; Ding, C. C.; Luo, X.; Cui, Y. B. et al. Electro-chemical nitrate remediation at lower concentrations: Efforts toward practical environmental applications. *Chin. Chem. Lett.* **2026**, *37*, 112141.
[26] Liu, H. L.; Zhang, S. Y.; Premy, T.; Zhang, C. P.; Liu, F. Y. Pulsed electrocatalysis on iron-decorated copper foam enables efficient and selective ammonia synthesis from low-concentration nitrate. *J. Environ. Chem. Eng.* **2025**, *13*, 118539.
[27] Xi, Z. C.; Su, J. H.; Yu, J. C.; Xu, X.; Jing, P.; Liu, B. C.; Zhang, J. Coupling oxygen vacancies-enriched nickel hydroxides with copper nanowires for tandem electrocatalysis in electrochemical nitrate reduction to ammonia. *J. Power Sources* **2026**, *666*, 239141.
[28] Song, Q. N.; Li, M.; Hou, X. S.; Li, J. C.; Dong, Z. J.; Zhang, S.; Yang, L.; Liu, X. Anchored Fe atoms for NO bond activation to boost electrocatalytic nitrate reduction at low concentrations. *Appl. Catal. B: Environ.* **2022**, *317*, 121721.
[29] Han, W.; Ge, X.; Yuan, J. L.; Pan, R. L.; Yang, Y.; Zou, G. L.; Xie, H. B. Spatial-confined effect of CuO_x microneedles bundles on TiO_2 nanotubes: Reinforcing the adsorption and enrichment of ultralow concentration nitrate for efficient NH_3 electrosynthesis. *Appl. Catal. B: Environ. Energy* **2025**, *361*, 124659.
[30] Zhao, X.; Chen, M. S.; Wang, D.; Zhang, H. R.; Hu, G. Z.; Zhou, Y. T. Ultrafine Nano-copper derived from dopamine polymerization & synchronous adsorption achieve electrochemical purification of nitrate to ammonia in complex water environments. *Chin. Chem. Lett.* **2024**, *35*, 109327.
[31] Zhou, J. J.; Zhu, Y. Q.; Wen, K. Y.; Pan, F.; Ma, H. R.; Niu, J. F.; Wang, C. Y.; Zhao, J. C. Efficient and selective electrochemical nitrate reduction to N_2 using a flow-through zero-gap electrochemical reactor with a reconstructed $Cu(OH)_2$ cathode: Insights into the importance of inter-electrode distance. *Environ. Sci. Technol.* **2024**, *58*, 4824–4836.
[32] Yu, J. C.; Xi, Z. C.; Su, J. H.; Jing, P.; Xu, X.; Liu, B. C.; Zhang, J. Enhancing electrocatalytic nitrate reduction performance of Co_3O_4 nanoneedle arrays by La-doping. *J. Rare Earths* **2025**, *43*, 1382–1389.
[33] Zhu, Y. Q.; Zhang, L. B.; Wen, K. Y.; Pan, F.; Dong, G. G.; Wang, H. L.; Yu, H. T.; Wang, C. Y. Preparation of Pocky-sticks like Ni_4N@Cu heterostructure cathode via *in-situ* electrochemical reconstruction for electrocatalytic nitrate reduction. *Sep. Purif. Technol.* **2025**, *361*, 131309.
[34] Chen, H.; Lin, C. Z.; Li, W. J.; Wang, R.; Feng, J. T.; Yan, W. Pulse driven and polypyrrole mediated microenvironment regulation synergistically achieve efficient conversion of nitrate to ammonia by copper oxide electrocatalsis. *Sep. Purif. Technol.* **2026**, *382*, 136168.
[35] Fan, X.; Lai, C.; Qin, L.; Zhang, M. M.; Yan, H. C.; Liu, S. Y.; Ma, D. S.; Liu, Q. T.; Tang, L. Oxygen vacancy-assisted CuCo tandem catalyst boosts efficient electrocatalytic neutral ultralow-concentration nitrate to ammonia. *Chem. Eng. J.* **2025**, *522*, 168046.
[36] Sun, Y. C.; Wang, N.; Sun, W. Z.; Li, C.; Zhong, B. W. Bifunctional porous copper nanosheets for versatile electrocatalytic nitrate reduction: From water remediation to resource recovery. *Chem. Eng. J.* **2025**, *524*, 169075.
[37] Chen, Y.; Xia, X. Y.; Tian, L.; Yin, M. Y.; Zheng, L. L.; Fu, Q.; Wu, D. S.; Zou, J. P. Constructing built-in electric field via CuO/NiO heterojunction for electrocatalytic reduction of nitrate at low concentrations to ammonia. *Chin. Chem. Lett.* **2024**, *35*, 109789.
[38] Hu, H. L.; Zhou, J. Y.; Hu, H. Y.; Wu, Y.; Wang, J. Y.; Du, M. L.; Lu, S. L. Interfacial enrichment by covalent organic framework microsphere layer enables efficient electrocatalytic nitrate reduction at low concentrations. *Chem. Eng. J.* **2026**, *529*, 172814.
[39] Wan, Y. C.; Pei, M. J.; Tang, Y. X.; Liu, Y.; Yan, W.; Zhang, J. J.; Lv, R. T. Interfacial water regulation for nitrate electroreduction to ammonia at ultralow overpotentials. *Adv. Mater.* **2025**, *37*, 2417696.
[40] Gu, L.; Song, N.; Wu, Z. Y.; Luo, H. X.; Chen, J.; Yang, J. P. Regulation of active hydrogen and nitrate concentration: Pulsed potential strategies in nitrate electroreduction microenvironments. *Angew. Chem., Int. Ed.* **2026**, *65*, e25547.
[41] Fan, J. L.; Arrazolo, L. K.; Du, J. X.; Xu, H. M.; Fang, S. Y.; Liu, Y.; Wu, Z. B.; Kim, J. H.; Wu, X. H. Effects of ionic interferents on electrocatalytic nitrate reduction: Mechanistic insight. *Environ. Sci. Technol.* **2024**, *58*, 12823–12845.
[42] Ji, Y. Y.; Niu, J. F.; Xu, D.; Wang, K. X.; Brejcha, J.; Jeon, S.; Warsinger, D. M. Efficient electrocatalysis for denitrification by using TiO_2 nanotube arrays cathode and adding chloride ions. *Chemosphere* **2021**, *274*, 129706.
[43] Ding, L.; Lan, H. S.; Li, X.; Zhao, Z. H.; Qu, Y. S.; Xia, Y. J.; Chang, X. H. Surface reconstruction induced Cu_2O/FeO heterojunction towards efficient nitrate-containing wastewater remediation. *J. Colloid Interface Sci.* **2025**, *690*, 137318.
[44] Feng, J. Y.; Chen, S. Y.; Chen, Y. C. Self-growing nitrogen doped cobalt-copper Co_4Cu_1N-CN/CF electrode for electrochemical nitrate removal. *J. Environ. Chem. Eng.* **2024**, *12*, 112686.
[45] Fu, W. Z.; Meng, G. Y.; Yin, D.; Zhang, X. W.; Shi, Y. Q.; Yang, Z. W.; Chang, D. M.; Chen, P.; Zhang, L. H. Electrodeposition of dense spherical Ni_3P on nickel foam cathode enhance nitrate electrochemical reduction via promoting nitrate adsorption. *J. Environ. Chem. Eng.* **2024**, *12*, 114815.
[46] Gao, Z. F.; Duan, X. Y.; Yin, X.; Li, W.; Zhu, H. W.; Wei, K. J.; Han, W. Q. Construction of electron-deficient Co on the nanoarrays enhances absorption and direct electron transfer to accelerate electrochemical nitrate reduction. *J. Hazard. Mater.* **2024**, *480*, 136443.
[47] Hu, J.; Zhao, T. T.; Li, X.; Hu, G. Z. Highly selective and efficient

electrocatalytic removal of low-concentration nitrate ions using self-supported porous $Ni_{0.8}Cu_{0.2}O$@CuO heterostructure arrays. *Sep. Purif. Technol.* **2023**, *325*, 124579.

[48] Li, D.; Zhang, X. Y.; Xie, J. F.; Chen, J. J.; Zhao, Q. B.; Liu, L.; Wang, W. K.; Li, W. W.; Yu, H. Q. Ultrathin cobalt-based nanosheets containing surface oxygen promoted near-complete nitrate removal. *J. Colloid Interface Sci.* **2024**, *672*, 383–391.

[49] Li, Z. Y.; Zhang, Y. G. Highly selective electrocatalytic nitrate reduction at P-doped CoO_x-derived PBAs self-supported nickel foam electrode. *J. Environ. Chem. Eng.* **2025**, *13*, 119243.

[50] Ma, X.; Zhong, J. P.; Wang, R. Y.; Li, D. X.; Li, K.; Luo, L. J.; Li, C. H. Zeolitic imidazolate framework derived Fe catalyst electrocatalytic-driven atomic hydrogen for efficient reduction of nitrate to N_2. *J. Hazard. Mater.* **2024**, *471*, 134354.

[51] Nguyen, T. N. T.; Mariappan, K.; Ahmad, M. S.; Tian, F. Z.; Tung, C. W.; Su, J. F.; Liu, C. L.; Chen, C. L. Enhanced electrochemical nitrate reduction: Geometrically tailored Pd/Cu electrodes for superior nitrogen selectivity. *J. Environ. Chem. Eng.* **2025**, *13*, 117833.

[52] Shen, S. Y.; Wang, S. Y.; Jia, Y. N.; Wu, B.; Tan, S. Y.; Chen, Q.; Zhang, B.; Zhao, X. S.; Sun, C.; Zhou, S. D. et al. Tailoring Ni 3D orbitals in Ni–Fe/Ni foam heterostructures for enhanced H* adsorption and boosted electrocatalytic nitrate reduction performance. *Sep. Purif. Technol.* **2024**, *349*, 127867.

[53] Zhao, T. T.; Hu, J.; Chang, F. Q.; Xie, X. S.; Zhao, X.; Abdukayum, A.; Gao, S. S.; Hu, G. Z. Self-supported copper/copper oxide microspheres for efficient electrocatalytic removal of low-concentration nitrate from aqueous solutions. *Sep. Purif. Technol.* **2025**, *354*, 128872.

[54] Zhou, J. J.; Pan, F.; Yao, Q. F.; Zhu, Y. Q.; Ma, H. R.; Niu, J. F.; Xie, J. P. Achieving efficient and stable electrochemical nitrate removal by *in-situ* reconstruction of Cu_2O/Cu electroactive nanocatalysts on Cu foam. *Appl. Catal. B: Environ.* **2022**, *317*, 121811.